

## RESEARCH ARTICLE

10.1002/2013JC009307

## Key Points:

- Observations document a 1.5Sv gyre dominating the upper 700 m of Pine Island Bay
- Export of ice-cavity water drives a boundary current along a glacier calving front
- Upwelling of ice-cavity water occurs partially within the shear margins of ice streams

## Correspondence to:

A. M. Thurnherr,  
ant@ldeo.columbia.edu

## Citation:

Thurnherr, A. M., S. S. Jacobs, P. Dutrieux, and C. F. Giulivi (2014), Export and circulation of ice cavity water in Pine Island Bay, West Antarctica, *J. Geophys. Res. Oceans*, 119, 1754–1764, doi:10.1002/2013JC009307.

Received 26 JULY 2013

Accepted 13 FEB 2014

Accepted article online 22 FEB 2014

Published online 11 MAR 2014

## Export and circulation of ice cavity water in Pine Island Bay, West Antarctica

A. M. Thurnherr<sup>1</sup>, S. S. Jacobs<sup>1</sup>, P. Dutrieux<sup>2</sup>, and C. F. Giulivi<sup>1</sup>

<sup>1</sup>Lamont-Doherty Earth Observatory, Columbia University, Palisades, New York, USA, <sup>2</sup>British Antarctic Survey, Natural Environment Research Council, Cambridge, UK

**Abstract** Large sectors of the Antarctic ice sheet are vulnerable to increases in melting at the bases of fringing ice shelves, with melt rates depending on ocean temperatures and circulations in the sub-ice cavities. Here we analyze an oceanographic data set obtained in austral summer 2009 in Pine Island Bay, which is bounded in the east by the calving front of the Amundsen Sea's fast-moving Pine Island Ice Shelf. The upper-ocean velocity field in the ice-free bay was dominated by a 700 m deep and 50 km wide gyre circulating 1.5 Sv of water clockwise around the bay. Ice cavity water was observed in a surface-intensified and southward-intensified boundary current along the ice front, and in a small ice cove at the end of the southern shear margin of the ice shelf. Repeat measurements in the cove reveal persistent cavity water export of  $\approx 0.25$  Sv during 10 days of sampling. Vertical velocities in the cove above the ice draft were dominated by buoyancy-frequency oscillations with amplitudes of several cm/s but without significant net upwelling. In combination with the seawater properties, this observation indicates that much of the upwelling occurs within fractured ice near the cove, potentially contributing to weakening the ice shelf shear margin.

### 1. Introduction

The Antarctic Ice Sheet is vulnerable to changes in ocean forcing of its fringing ice shelves [Joughin *et al.*, 2012]. Grounded ice sheets are dynamic entities, mainly gaining mass from precipitation and losing it by export to the sea in embedded glaciers (ice streams). Seaward of the grounding zones where those ice streams lose contact with the seabed, they become floating ice shelves which terminate in iceberg calving fronts. Some of the cavities underneath floating ice shelves are known to host overturning circulations fed by comparatively warm Circumpolar Deep Water (CDW), which flows at depth toward the back of the cavities. The overturning is driven by rapid melting near deep grounding lines, where cooler, fresher, and less dense mixtures of CDW and meltwater are produced. The buoyant waters rise and flow toward the calving fronts, sculpting networks of channels into the ice [e.g., Stanton *et al.*, 2013; Dutrieux *et al.*, 2013]. In regions where exported ice cavity water (ICW) retains sufficient buoyancy at the calving fronts, it rises toward and sometimes reaches the sea surface [e.g., Mankoff *et al.*, 2012].

The mass balance of Antarctic glaciers and ice streams is important because the ice sheet provides land storage for immense amounts of water that can significantly affect global sea level [Church *et al.*, 2001]. While the mass balance of any given glacier is complex, evidence has been mounting for links between stronger ocean circulation coupled with increased subsurface temperatures, increased melting of ice shelves, and the thinning and acceleration of their incoming ice streams [Joughin *et al.*, 2012]. The West Antarctic Ice Sheet is of particular interest because much of its ice rests on a bed grounded below sea level and deepening landward, a setup that can lead to runaway ice sheet retreat as melting weakens the buttressing provided by its ice shelves [Schoof, 2007]. Considerable attention has been directed toward its Pine Island Glacier (PIG), a fast-moving ice stream that evolves into the Pine Island glacier Ice Shelf (PIIS), which terminates in Pine Island Bay (PIB) in the southeast Amundsen sea [Jacobs *et al.*, 1996; Rignot, 2008; Jenkins *et al.*, 2010; Joughin *et al.*, 2010; Bindshadler *et al.*, 2011]. Based primarily on ocean measurements from 1994 through 2009 along the PIIS calving front, changes of  $\approx 50\%$  in meltwater production have been inferred [Jacobs *et al.*, 2011; Dutrieux *et al.*, 2014]. Additionally, in summer 2009, a striking cyclonic gyre was observed to occupy a large fraction of the surface area of the ice-free PIB [Jacobs *et al.*, 2011; Mankoff *et al.*, 2012; Tortell *et al.*, 2012].

The primary objective of the present work is to obtain a better understanding of the seawater flows to and from the cavity beneath the Pine Island Ice Shelf by also including many of the 2009 CTD and ADCP

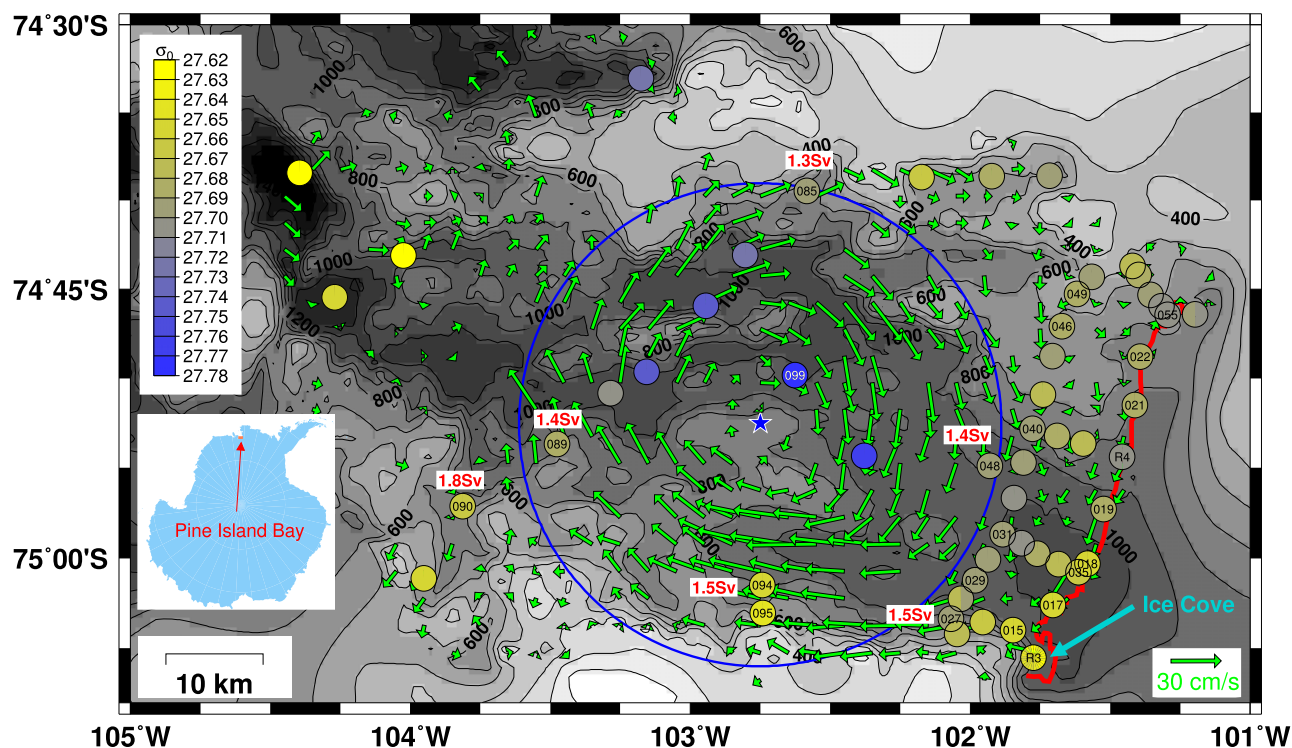


**Figure 1.** Observations in Pine Island Bay (inset), including topography (gray-shaded contours; *Nitsche et al.* [2007]), Pine Island Glacier calving front (red line), near-surface velocity field (green arrows), radial gyre transport above 700m (red labels), and potential density anomaly between 500 and 550 m (colored bullets). Arrows show SADCPC velocities averaged between 30 and 300m and gridded into  $\approx 3 \times 3$  km horizontal boxes. The large blue circle indicates the approximate extent of the gyre dominating the upper-ocean circulation in PIB, with the blue star marking its center. Numbered CTD station bullets are discussed in the text; “R” labels indicate repeat stations.

measurements (section 2), not utilized in the earlier studies. Away from the immediate vicinity of the PIG calving front, the horizontal circulation in PIB was dominated by a geostrophic gyre recirculating  $\approx 1.5$  Sv of water around the bay (section 3). Near the southeast corner of PIB, the recirculating water in the gyre was joined by recently formed ICW flowing out of a small cove near the southern end of the calving front (section 4) and by a southward coastal boundary current carrying the export flux from the remainder of the front (section 5). The manuscript concludes with a discussion of the main results (section 6).

## 2. Data and Methods

From 16 to 31 January 2009, the R/V Nathaniel B. Palmer carried out an oceanographic survey of PIB, with CTD/O<sub>2</sub>/LADCP (Lowered Acoustic Doppler Current Profiler) stations concentrated along transects near the calving front of the PIIS, with the closest line of stations taken  $\approx 500$  m from the ice (Figure 1). Near-continuous upper-ocean velocity measurements were also obtained along the cruise track using a ship-mounted ADCP (SADCPC) system. The only operating SADCPC, a Teledyne/RDI 150 kHz instrument, yielded good data spanning the depth range between 30 and 300 m. The profiling platform consisted of a SeaBird 9+ CTD mounted on a frame together with a rosette and a Teledyne/RDI Workhorse 300 kHz ADCP pointing downward. The CTD was equipped with a sensor for pressure and dual sensors for temperature, conductivity, and oxygen concentration, monitored by water sampling and calibrated before and after the cruise. The CTD/O<sub>2</sub> data were processed, edited, and reported to the National Oceanographic Data Center according to standard procedures to accuracies of  $\approx 0.002$  in salinity,  $0.002^\circ\text{C}$  in temperature, and  $2 \mu\text{mol kg}^{-1}$  in dissolved oxygen. The LADCP was programmed to collect single-ping velocity “ensembles” in beam coordinates. A bin length of 8 m was chosen, the blanking distance set to zero, and the data from the first bin were discarded before processing. In order to minimize the effects of previous-ping interference from the seabed, alternating ping intervals of 1.5 and 2 s were used. Full-depth profiles of horizontal velocity were derived with version IX\_9 of the LDEO implementation of the velocity inversion method [*Visbeck*, 2002], accurate to  $\approx 3 \text{ cm s}^{-1}$  under typical conditions [*Thurnherr*, 2010]. No detiding was applied to the velocity

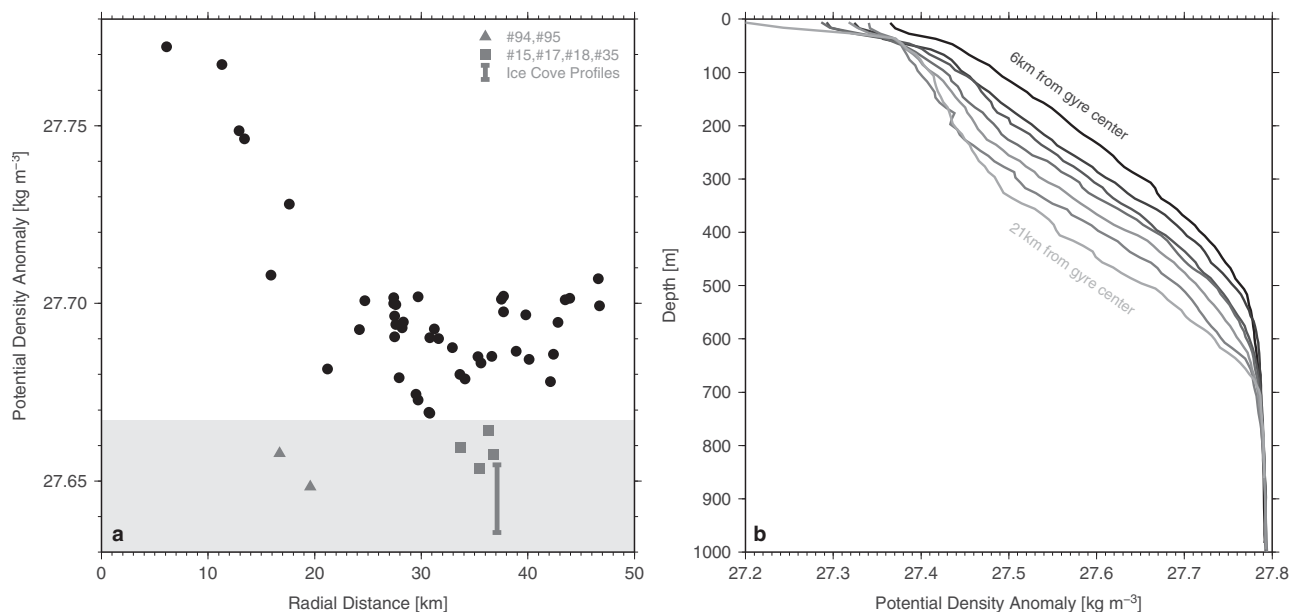


**Figure 2.** PIB gyre density structure. (a) Mean potential density between 500 and 550 m (subset of colored bullets in Figure 1) versus distance from the gyre hub (star in Figure 1). Anomalous low densities shown in grey are affected either by topography constraining the gyre (#94 and #95) or by outflow of ice-cavity water (remaining samples); see text for details. Profiles west of 103°30'W and north of 74°35'S are considered outside of PIB proper and not shown in this figure. (b) Potential-density profiles in the gyre core, corresponding to black bullets at radial distance <22 km in Figure 2a.

data used here. Vertical-velocity profiles were derived from the same data by subtracting the vertical package motion, determined from the CTD pressure time series, from the ADCP-derived vertical velocity measurements to an accuracy of 2–3 mm s<sup>-1</sup> [Thurnherr, 2011]. Since most of the profiles in the present data set were collected with little instrument motion due to surface waves, the stated accuracies of the LADCP velocities are likely conservative.

### 3. A Gyre in Pine Island Bay

During late January 2009, the upper-ocean velocity field in PIB was dominated by a coherent closed cyclonic gyre centered around 74°52.5'S 102°45'W (Figure 1) [see also Jacobs *et al.*, 2011, Figure 2; Mankoff *et al.*, 2012, Figure 4; Tortell *et al.*, 2012, Figure 13]. Earlier evidence for a similar gyre is also apparent in a 1994 CTD data set from PIB [Hellmer *et al.*, 1998, Figure 2]. Schodlok *et al.* [2012] also discuss a cyclonic gyre that appears in their modeled circulation of PIB. However, their definition of PIB covers the full continental shelf area from ≈100° to 115°W. What they call the “main part” of their gyre is centered between 72° and 73°S, i.e., several hundred km to the north of our study region. The PIB gyre discussed here is what Schodlok *et al.* [2012] refer to as “the smaller gyre just outside the PIG cavity.”

Both the horizontal velocities near the sea surface and the density field in the lower part of the gyre suggest coherent rotation extending out to a radial distance of ≈25 km from the center (Figure 1). At greater distances, the horizontal circulation appears less “gyre like,” with horizontal density gradients unaligned with the radial gyre direction, in particular near the ice shelf front. The density data in Figure 2 support these visual inferences, as density decreases nearly uniformly from the gyre center out to ≈25 km, where it levels off. Waters with anomalously low densities near 500 m were observed close to the ice front south of 75°S (grey squares in Figure 2a), inside a small ice cove (vertical bar), and near the southern edge of the bay where the gyre was topographically constrained (grey triangles). The gyre's vertical extent was well defined from the surface to 700 m (Figure 2b).

Above 50 m, the density was affected by surface effects and below 700 m the density field was horizontally nearly uniform, indicating weak geostrophic vertical shear below that depth. The LADCP data also show weak vertical shear and small horizontal velocities below 700 m everywhere in PIB—3.6 cm s<sup>-1</sup> *rms* speed in the profiles within the large blue circle—implying that a level of no motion at or below 700 m is

adequate to estimate geostrophic velocities in the upper ocean. Consistent with this inference, geostrophic calculations of the azimuthal gyre flow in the upper ocean agree well with SADCPC measurements (not shown). Calculations of cyclonic transport above 700 m between the gyre center and its nominal perimeter at 25 km yield approximately uniform estimates along its circumference (red labels in Figure 1). The LADCP velocities below 700 m are not random, however. Seven out of the nine profiles within the nominal gyre boundary show eastward flow (i.e., toward the ice-shelf cavity) in the vertically averaged velocities below 700 m whereas there is no discernible pattern in the corresponding meridional velocities (not shown).

#### 4. Horizontal and Vertical Velocities in a Small Ice Cove

PIB is bounded in the east by the calving front of the PIIS (red line in Figure 1). Based on CTD profiles near the ice front from the same data set analyzed here, *Jacobs et al.* [2011] infer an overturning circulation in the ice cavity underneath the PIIS, fed by an inflow of dense, warm, oxygen-poor CDW, and yielding a cooler and less salty return mixture of less dense CDW and meltwater, which we are calling ICW. While evidence for ICW export can be found along the entire southern half of the ice front (Figure 3 and section 5), upper-ocean velocities directed away from the ice were only measured near a small cove at the southern end of the PIIS front ("R3" in Figures 1 and 3), where *Jacobs et al.* [2011] found essentially undiluted ICW. SADCPC data in and near this cove, nearly surrounded by glacial ice, show persistent westward flow through its  $\approx 3.6$  km wide opening to PIB.

Outflow from the cove can be investigated in greater detail by using 26 LADCP/CTD profiles taken there (Figure 4): profile #16 on 18 January, 24 "yo-yo" profiles (#58–#81) at hourly intervals on 24–25 January, and #93 on 28 January. Ensemble averages constructed from those cove profiles (heavy lines) indicate that the

outflow likely persisted over that 10 day interval, extended from the sea surface down to  $\approx 500$  m, and was associated with vertical velocities of both signs. The full water-column average along-outflow and vertical velocities in the ice cove were  $10.5 \pm 1.3 \text{ cm s}^{-1}$  and  $0.0 \pm 0.7 \text{ cm s}^{-1}$ , respectively, indicating approximately steady net outflow during the measurement period. (For comparison, version 2.01 of the Circum-Antarctic Tidal Simulation model of *Padman et al.* [2002] predicts  $0.6 \text{ cm s}^{-1}$  rms barotropic tidal speed for the PIB stations shown in Figure 1.) Above the draft of the surrounding ice, the amount of ICW exported from the cove can be estimated by evaluating

$$Q_x(z_d) = \int_0^{z_d} u(z)l(z)dz, \quad (1)$$

where  $z_d$ ,  $u(z)$ , and  $l(z)$  denote ice draft (with  $z$  increasing downward), lateral average outflow velocity, and width of the cove opening, respectively. Assuming steep ice walls below the sea surface [ $l(z) \approx 3.6 \text{ km}$ ], export fluxes as a function

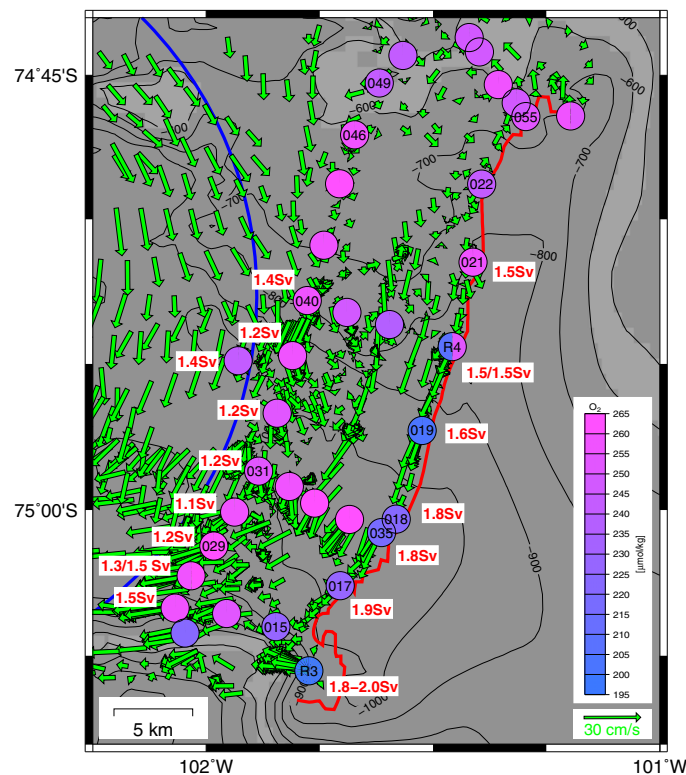


**Figure 3.** Circulation and upper-ocean oxygen concentration near the front of the Pine Island Ice Shelf (red line). Station bullets are shaded according to the mean oxygen concentration between the 27.4 and 27.6 isopycnal surfaces ( $\approx 100$ –500 m) and labeled as in Figure 1. The blue line shows the nominal extent of the PIB gyre (25 km radius). Green arrows show the vertically averaged SADCPC velocities between 30 and 300 m, without spatial gridding. Red numbers show integrated geostrophic transports above 700 m between the gyre center (#99, Figure 1) and the stations closest to the labels; repeat stations have multiple values.

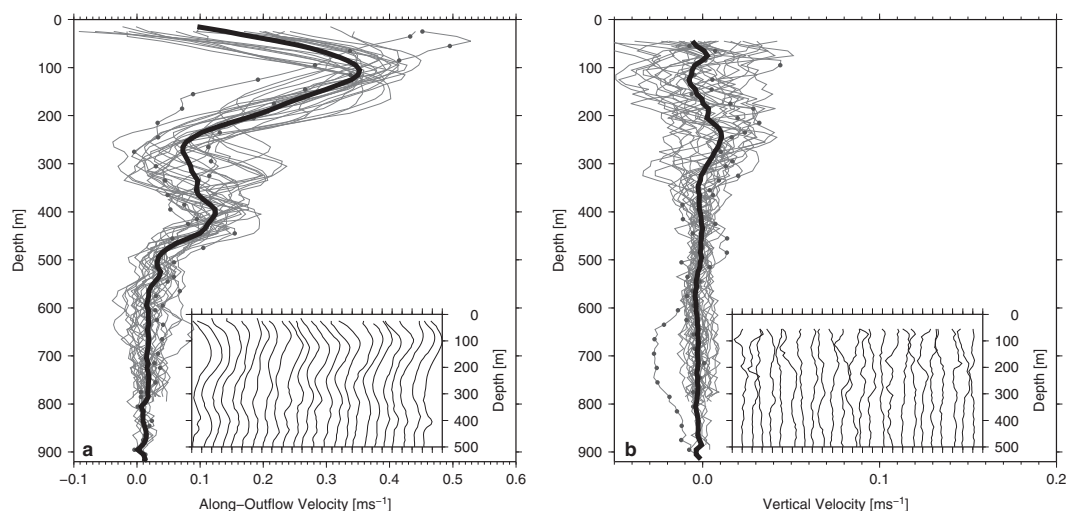


**Figure 4.** LADCP velocities from the ice cove profiles #16, #58–#81, and #93 (“R3” in Figures 1 and 3). Main panels show both ensemble-average (heavy black) and individual profiles (grey); profiles #16 and #93, not part of the 24 h yo-yo station, are marked with bullets. Insets show waterfall plots of the hourly yo-yo profiles (#58–#81). (a) Horizontal velocities projected onto the along-outflow direction (280° true). (b) Downcast vertical velocities.

of ice draft were calculated from the mean yo-yo, and from the two flanking profiles. Using 200–500 m as the likely range of ice drafts near the cove [Mankoff *et al.*, 2012] yields transport estimates ranging between 0.15 and 0.35 Sv for ICW export from the cove.

In contrast to the weak barotropic variability on the time scales resolved by our survey, both horizontal and vertical velocities in the ice cove displayed baroclinic temporal variability with amplitudes of several  $\text{cm s}^{-1}$  and vertical scales ranging from 10 s to 100 s of meters (grey profiles in Figure 4). The hourly yo-yo repeat profiles (insets in the figure) reveal distinct time scales for the horizontal and vertical flow variability. Compared to the 1 h sampling interval of the yo-yo profiles, the long time scale of the horizontal outflow velocity variability is evidenced by the slow vertical phase propagation in the waterfall plot. On the other hand, little apparent coherence between subsequent hourly vertical-velocity samples suggests that vertical-velocity variability in the ice cove is either associated with time scales shorter than 1 h or dominated by measurement noise. In order to distinguish between these possibilities, the 24 hourly yo-yo profiles were used to estimate the vertical-velocity autocorrelation

$$R(\tau) = \frac{\langle\langle w(t, z) - \langle w(z) \rangle \langle w(t + \tau, z) - \langle w(z) \rangle \rangle\rangle}{\sigma_w(z)^2}, \quad (2)$$

where  $w(t, z)$  and  $w(t + \tau, z)$  are the two vertical-velocity measurements from depth  $z$  during each down-upcast sequence,  $\tau$  is the time lag between the two samples,  $\sigma_w(z)$  is the standard deviation of vertical velocity calculated from all 24 yo-yo casts, and  $\langle \rangle$  indicates ensemble averaging. Figure 5 shows the resulting vertical-velocity autocorrelation for three different depth ranges (depth is correlated with time lag  $\tau$  because of the down-upcast sampling pattern). Since the three layer-averaged autocorrelations are mutually consistent, indicating strong negative correlations peaking at half a buoyancy period, we conclude that the vertical velocity measurements taken in the ice cove during the 24 h yo-yo repeat station are not dominated by noise, but by a process with a time scale close to the buoyancy period  $\tau \approx 32$  min. As an aside, we note that the high-frequency variability in both the horizontal and vertical velocity ice cove measurements is consistent with internal gravity waves. In particular, observations and theoretical considerations suggest that low-frequency (near-inertial) waves typically dominate the temporal variability of horizontal velocity, whereas the vertical velocities are dominated by high-frequency (near- $N$ ) waves [Desaubies, 1975]. Both the amplitudes (several  $\text{cm/s}$ ) and vertical scales (tens to hundreds of meters) of the high-frequency variability are also consistent with the large base of “finescale” observations that are typically ascribed to internal waves [e.g., Kunze *et al.*, 2006].

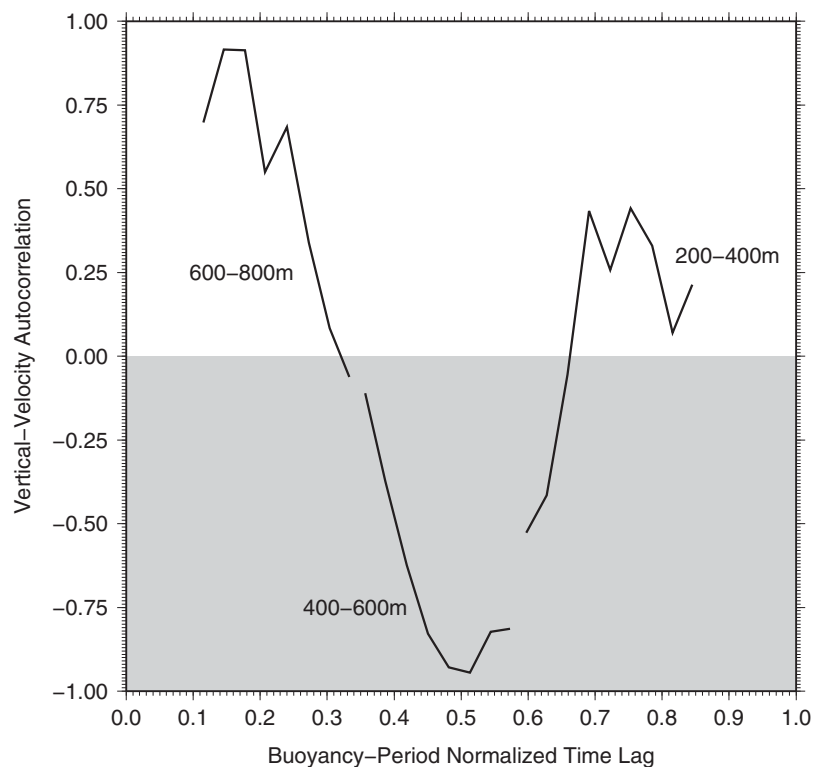


**Figure 5.** Normalized vertical-velocity autocorrelations from the yo-yo profiles #58–#81 obtained in the ice cove. The time axis is normalized by the buoyancy period near the middle of the profile at 500 m, where the density stratification has a maximum ( $N \approx 3.3 \times 10^{-3} \text{ rad s}^{-1}$ ;  $\tau \approx 32 \text{ min}$ ). The three line segments show separate autocorrelation estimates binned in 1 min averages from the depth ranges indicated; averages from bins with fewer than 15 samples are not shown.

## 5. Circulation and Hydrography Along the Ice Front

Jacobs *et al.* [2011] infer that export of ICW from the ice cavity during the cruise took place primarily south of station #19, with inflow into the cavity north of that station. The SADC data near the ice front show weak and variable upper-ocean velocities off the northern part of the calving front and a southward-increasing along-ice flow in the south (Figure 3), as would be expected for a southward flowing boundary current along the ice, fed by outflow from the PIIS cavity. Geostrophic velocity profiles between station pairs from two quasi-meridional sections along the ice (Figure 6) show the southward along-ice current along the entire ice front gradually deepening and strengthening along its path, reaching peak speeds of  $30 \text{ cm s}^{-1}$  and extending down to  $\approx 700 \text{ m}$  in the southeast corner of PIB. (For comparison, the subsurface ice topography near the front is known to be irregular, with typical drafts of  $350 \pm 100 \text{ m}$  [Mankoff *et al.*, 2012].) The reasonable agreement between SADC velocities and the corresponding geostrophic estimates confirm that a 700m level of no motion is adequate for determining the first-order structure of the along-ice flow, although uncertainties remain regarding its strength, especially to the north where velocities are low. The geostrophic estimates imply that transport between the edge of PIB gyre and the ice front increases monotonically by about  $0.4 \text{ Sv}$  southward along the calving front (red numbers in Figure 3). Near the southeast corner of PIB, both the along-ice boundary current and outflow from the ice cove (section 4) join the southwestward transport of the PIB gyre. The combined westward flow is topographically constrained along the southern margin of PIB, where the nominal gyre limit extends into water shallower than 300 m, increasing the velocities (Figure 1) and steepening the radial density gradients associated with the gyre flow (exemplified in Figure 2 by the anomalously low densities in profiles #94 and #95).

Because of comparatively low dissolved oxygen in CDW, that signature in the upwelled ICW is clearly apparent in the upper-ocean oxygen distribution along the southern half of the PIIS front (Figure 3). CTD profiles show that its high-temperature and low-oxygen anomalies are limited to depths shallower than 400 m (i.e., above the ice draft), whereas horizontal property variability is minimal below 500 m (Figure 7). Except for profiles in the ice cove (red), all those with meltwater signatures (orange) show vertically stacked

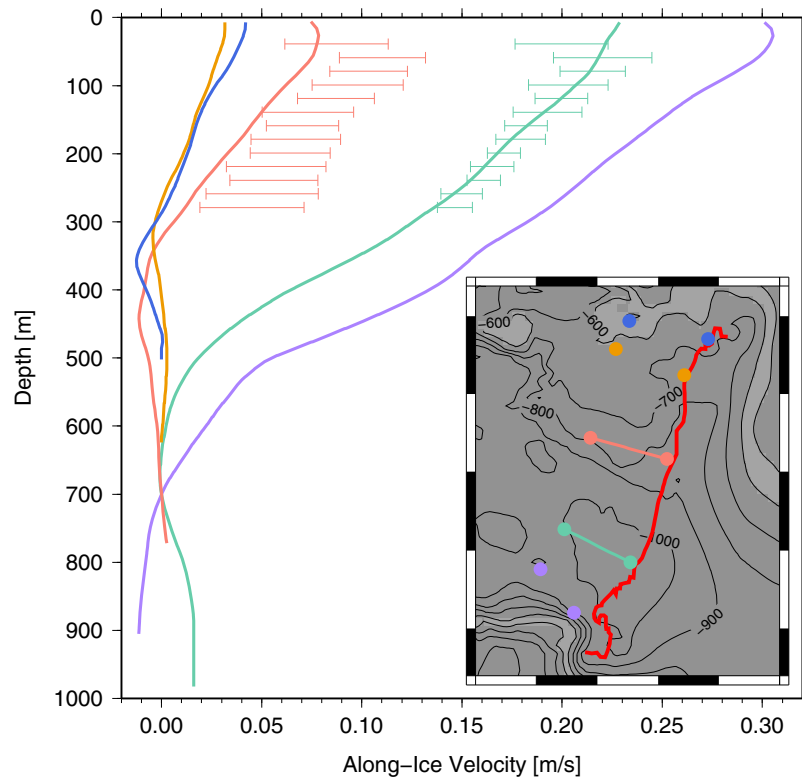


**Figure 6.** Main figure: Southward along-ice velocities between station pairs off the PIIS; solid lines show geostrophic profiles referenced to 700 m; error bars show bootstrapping-derived 95% confidence intervals from section-averaged SADCPC velocities between station pairs connected by straight ship track. Inset: Map, as in Figure 3, with color-coded station positions (bullets) and SADCPC sections (lines).

interleaving layers of ICW and background waters above the ice draft. Ice cove oxygen concentrations remain uniformly low up to  $\approx 100$  m, i.e., the properties of the entire cove water column were consistent with ICW except for a top layer presumably altered by surface effects such as air-sea interaction and biological processes. ICW in the cove was also anomalously low in density between  $\approx 400$  and 550 m, relative to background water at the same depths (Figure 7c; see also Figures 1 and 2).

While the distribution of ICW along the PIIS front and the southward strengthening of the along-ice boundary current are consistent with the geostrophic inference of *Jacobs et al.* [2011] that ICW export is concentrated in the southern half of the front, the LADCP-derived cross-ice-edge velocities reveal a more complex picture with instantaneous flows both toward and away from the ice along the entire front (Figure 8a). The

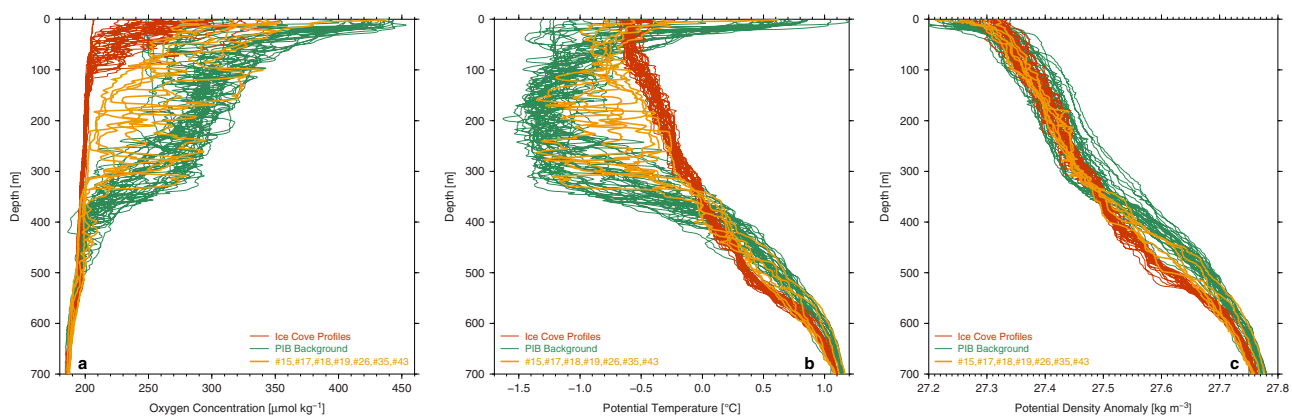


**Figure 7.** (a) Dissolved oxygen, (b) potential temperature, and (c) potential density profiles along the ice front (station map in Figure 3). Red profiles are from the ice cove; profiles #15, #17–#19, #26, #35, and #43 (one of the “R4” repeat profiles) with clear meltwater signatures are orange; remaining profiles are green. (For a T/S diagram constructed from a subset of the same data, see *Jacobs et al.* [2011, Figure 3b].)

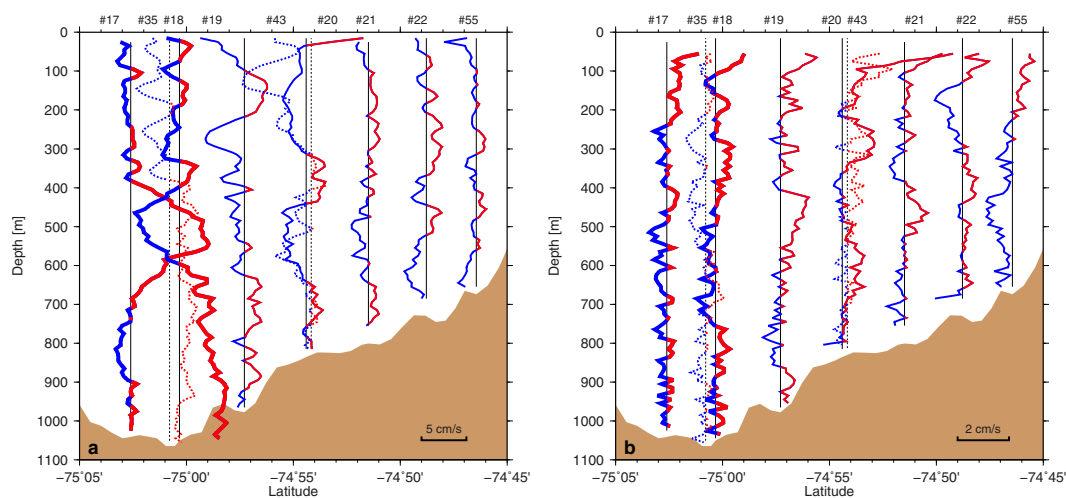


**Figure 8.** LADCP profiles along the PIIS front (station map in Figure 3), with red and blue indicating positive and negative velocities, respectively; dotted lines distinguish nearby profiles, and profiles #17 and #18 are marked with extraheavy lines. (a) Horizontal velocities projected individually onto the local cross-frontal direction; positive toward the ice. (b) Downcast vertical velocities.

strongest cross-frontal velocities ( $\approx 10 \text{ cm s}^{-1}$ ) were observed 5.5 km apart in profiles #17 and #18 in two opposing “jets” located between 400 and 600 m, i.e., just below the ice draft. Comparing the downcast and upcast profiles on each cast, neither jet changed significantly during the elapsed 30 min. In contrast, velocity differences exceeding  $5 \text{ cm s}^{-1}$  would be expected if the variability between profiles #17 and #18 were due to temporal variability alone (100 min between the upcast sampling of the “jets” in #17 and the downcast sampling in profile #18). The lack of similarly enhanced horizontal flow in the same depth range in profile #19, obtained less than 2 h and 6 km from #18 suggests a horizontal scale less than 10 km for the dynamical feature giving rise to the observed jets. Taken together, we hypothesize that the jets are signatures of a coherent, anticyclonic, submesoscale vortex straddling the ice edge.

Outside this submesoscale vortex, both the horizontal and the vertical velocities from the ice edge show similar patterns (Figure 8). They are dominated by currents with vertical scales ranging from a few tens to hundreds of meters. Similar to the velocity observations from the ice cove (section 4), the vertical-velocity autocorrelation estimated from the ice front profiles is consistent with motions near the buoyancy frequency, whereas horizontal velocity varies on longer time scales (not shown).

## 6. Discussion

From a subset of the CTD profiles analyzed here, *Jacobs et al.* [2011] infer a melt-driven overturning circulation in the ice cavity, characterized by deep inflow of warm, salty CDW and shallow outflow of a less dense melt-modified deep water (ICW). Numerically modeling ocean circulation in the cavity, *Payne et al.* [2007] find that buoyant, melt-laden plumes flow along inverted channels in the base of the ice shelf toward the ice front with the southernmost channel carrying the bulk of the flow. Observational support for their cavity circulation includes “three reasonably persistent polynyas” coinciding with the locations of modeled outflows. *Bindschadler et al.* [2011] and *Mankoff et al.* [2012] confirm this inference using additional satellite images, noting that the southernmost polynya is usually the largest. While there were no small, coastal polynyas in the ice-free Pine Island Bay during January 2009, the ice cove coincided with the location of the southern polynya. In the velocity data analyzed here, there are no indications for concentrated ICW outflow near the central and northern polynya sites (near our stations #19 and #55, respectively.)

The partially enclosed setting and persistently strong outflow velocities help to constrain ICW export from the southern ice cove/polynya site. We take the resulting estimate of  $0.25 \pm 0.10 \text{ Sv}$  as a lower bound for the total ICW export, since it does not include ICW leakage into PIB along the remainder of the PIIS front. That more distributed contribution to the ICW export is harder to constrain, but the streamwise strengthening of the southward along-ice boundary current provides an upper bound of  $\approx 0.4 \text{ Sv}$ . Taken together, these estimates are comparable with the  $0.4 \text{ Sv}$  geostrophic estimate of *Jacobs et al.* [2011], and both analyses agree that

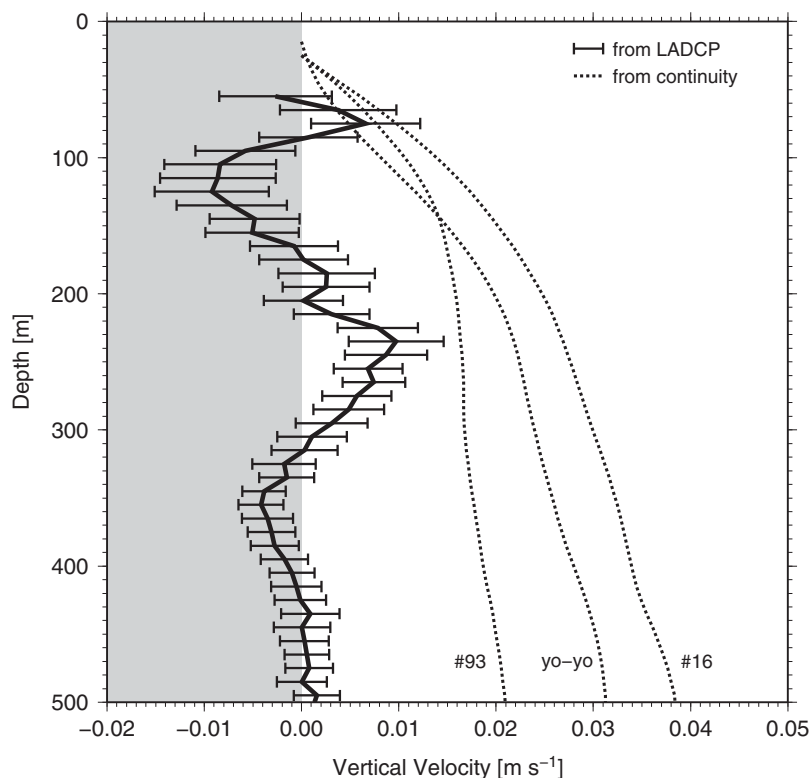


**Figure 9.** Vertical velocity in the ice cove. Error bars show the observed mean (as in Figure 4) with standard errors; the dotted lines show the upwelling required to replenish the water exported horizontally from the ice cove, if the ice walls were impenetrable and if the upwelling was uniform across the cove; see text for details.

exported ICW was advected away from the ice primarily in the upper ocean along the southern half of the PIIS front. The exported ICW joined the upper-ocean circulation of Pine Island Bay, dominated in late January 2009 by a cyclonic gyre, whose striking signatures in density, near-surface velocity, and sea-surface temperature have been noted before [Jacobs *et al.*, 2011; Tortell *et al.*, 2012; Mankoff *et al.*, 2012].

In order to understand the relationship between overturning under the ice shelf and the horizontal circulation in PIB, it is important to know how the gyre and the along-ice boundary current are driven. Buoyancy forcing by exported ICW is likely, as both the ice-front current and the southward-moving eastern limb of the gyre flow in the direction expected for buoyancy-driven coastal currents in the southern hemisphere. Predominant winds from the southeast during the cruise would have enhanced upwelling along the ice front, providing additional forcing in the same direction. These inferences are consistent with the numerical model of Heimbach and Losch [2012], which, without any wind forcing, reproduces a cyclonic gyre of  $\approx 0.4$  Sv in PIB, considerably weaker than the  $\approx 1.5$  Sv gyre in our observations. Since PIB is ice covered during most of the year, and its seawater was relatively warm in the summer of 2009 [Jacobs *et al.*, 2011], a weaker gyre may be more common.

The 2009 LADCP/CTD data also provide novel insight about ICW upwelling into the near surface layers of PIB. ICW is generated in the PIIS cavity beneath the ice, but is exported horizontally from the ice cove at shallower levels and must be continuously replenished. If the lateral ice walls of the cove were impenetrable, the ICW would have to upwell from below the basal ice. For such a setting, the mean vertical velocity in the cove above the ice draft can be estimated from continuity, i.e.,

$$w(z_d)A_s = Q_x(z_d), \quad (3)$$

where  $A_s = 9 \text{ km}^2$  is the horizontal surface area of the cove, assuming steep ice walls. Applying expressions 1 and 3 to the cove outflow profiles yields vertical velocities increasing monotonically from zero at the sea surface to  $2\text{--}4 \text{ cm s}^{-1}$  near 500 m (Figure 9). In contrast, the observed mean (i.e., subinertial) vertical velocity



**Figure 10.** Fractured and caved ice walls surrounding the ice cove at the terminus of the southern shear margin of the PIIS. Photograph by Maria Stenzel.

field in the cove shows both upwelling and downwelling layers above 500 m with zero mean and peak speeds of  $\approx 1 \text{ cm s}^{-1}$  ( $\bar{w} = 0.0 \pm 4.5 \text{ mm s}^{-1}$ ), and weaker vertical motion below that depth ( $\bar{w} = -0.2 \pm 1.0 \text{ mm s}^{-1}$ ). From the apparent correlation between mean  $w$  and outflow velocities above 500 m (Figure 4), we interpret these alternating vertical velocity layers as signatures of vertical divergence associated with the vertical structure of the outflow.

From the lack of net upwelling in the vertical velocity measurements, we infer that the ICW exported from the ice cove was replenished either by upwelling closer to the ice walls than was sampled or primarily by lateral flows. While our data do not preclude the former possibility, we consider the latter more likely, in particular because the fractured walls provide open channels for horizontal inflow into the ice cove from many directions (Figure 10, noting in particular the daylight at the end of one tunnel). Finding no indications in the property or velocity data for inflow of PIB water into the cove, we hypothesize that the water exported from the cove was replenished mainly by lateral flow of previously upwelled ICW through the fractured ice-cove walls. With outflowing ICW  $1\text{--}2^\circ\text{C}$  above freezing, the upwelled water retains sufficient heat to continue melting the fractured ice and possibly contributes to the weakness of the shear margin of the Pine Island ice shelf. While the inferences drawn here are based on only two weeks of sampling, the presence of quasi-persistent polynyas off the two shear margins of the ice shelf suggest that the situation encountered in summer 2009 may not have been exceptional.

#### Acknowledgments

Funding for collection and analysis of the 2009 data was provided by the National Science Foundation under grant ANT-06-32282, and by the Lamont-Doherty Earth Observatory. Detailed comments by an anonymous reviewer and by Robin Muench are gratefully acknowledged.

#### References

- Bindschadler, R., D. G. Vaughan, and P. Vornberger (2011), Variability of basal melt beneath the Pine Island Glacier ice shelf, West Antarctica, *J. Glaciol.*, *57*, 581–595.
- Church, J. A., J. M. Gregory, P. Huybrechts, M. Kuhn, K. Lambeck, M. T. Nhuan, D. Qin, and P. L. Woodworth (2001), Observed climate variability and change, in *Climate Change: The Scientific Basis. Contribution of Working Group I to the Third Assessment Report of the Intergovernmental Panel on Climate Change*, Chap. 2, edited by J. T. Houghton et al., pp. 99–183, Cambridge Univ. Press, Cambridge, U. K.
- Desaubies, Y. J. F. (1975), A linear theory of internal wave spectra and coherences near the Väisälä frequency, *J. Geophys. Res.*, *80*, 895–899.
- Dutrieux, P., D. G. Vaughan, H. F. J. Corr, A. Jenkins, P. R. Holland, I. Joughin, and A. H. Fleming (2013), Pine Island glacier ice shelf melt distributed at kilometre scales, *Cryosphere*, *7*, 1543–1555.
- Dutrieux, P., J. De Rydt, A. Jenkins, P. R. Holland, H. K. Ha, S. H. Lee, E. J. Steig, Q. Ding, E. P. Abrahamsen, and M. Schroder (2014), Strong sensitivity of Pine Island ice-shelf melting to climatic variability, *Science* *3(7)*, 468–472.
- Heimbach, P., and M. Losch (2012), Adjoint sensitivities of sub-ice shelf melt rates to ocean circulation under Pine Island Ice Shelf, West Antarctica, *Ann. Glaciol.*, *53*, 59–69.
- Hellmer, H. H., S. S. Jacobs, and A. Jenkins (1998), Ocean erosion of a fast-moving Antarctic glacier in the Amundsen Sea, in *Ocean Ice and Atmosphere*, *Ant. Res. Ser.*, vol. 75, edited by S. S. Jacobs and R. F. Weiss, pp. 83–99, AGU, Washington, D. C.
- Jacobs, S. S., H. H. Hellmer, and A. Jenkins (1996), Antarctic ice sheet melting in the Southeast Pacific, *Geophys. Res. Lett.*, *23*, 957–960.
- Jacobs, S. S., A. Jenkins, C. F. Giulivi, and P. Dutrieux (2011), Stronger ocean circulation and increased melting under Pine Island Glacier ice shelf, *Nat. Geosci.*, *4*, 519–523.
- Jenkins, A., P. Dutrieux, S. S. Jacobs, S. D. McPhail, J. R. Perrett, A. T. Webb, and D. White (2010), Observations beneath Pine Island Glacier in West Antarctica and implications for its retreat, *Nat. Geosci.*, *3*, 468–472.
- Joughin, I., B. E. Smith, and D. M. Holland (2010), Sensitivity of 21st century sea level to ocean-induced thinning of Pine Island Glacier, Antarctica, *Geophys. Res. Lett.*, *37*, L20502, doi:10.1029/2010GL044819.
- Joughin, I., R. B. Alley, and D. M. Holland (2012), Ice-sheet response to oceanic forcing, *Science*, *338*, 1172–1176.
- Kunze, E., E. Firing, J. M. Hummon, T. K. Chereskin, and A. M. Thurnherr (2006), Global abyssal mixing inferred from Lowered ADCP shear and CTD strain profiles, *J. Phys. Oceanogr.*, *36*, 1553–1576.

- Mankoff, K. D., S. S. Jacobs, S. M. Tulaczyk, and S. E. Stammerjohn (2012), The role of Pine Island Glacier ice shelf basal channels in deep-water upwelling, polynyas and ocean circulation in Pine Island Bay, Antarctica, *Ann. Glaciol.*, *53*, 123–128.
- Nitsche, F. O., S. S. Jacobs, R. D. Larer, and K. Gohl (2007), Bathymetry of the Amundsen Sea continental shelf: Implications for geology, oceanography, and glaciology, *Geochem. Geophys. Geosyst.*, *8*, Q10009, doi:10.1029/2007GC001694.
- Padman, L., H. A. Fricker, R. Coleman, S. Howard, and L. Erofeeva (2002), A new tide model for the Antarctic ice shelves and seas, *Ann. Glaciol.*, *34*, 247–254.
- Payne, A. J., P. R. Holland, A. P. Shepherd, I. C. Rutt, A. Jenkins, and I. Joughin (2007), Numerical modeling of ocean-ice interactions under Pine Island Bay's ice shelf, *J. Geophys. Res.*, *112*, C10019, doi:10.1029/2006JC003733.
- Rignot, E. (2008), Changes in West Antarctic ice stream dynamics observed with ALOS PALSAR data, *Geophys. Res. Lett.*, *35*, L12505, doi: 10.1029/2008GL033365.
- Schodlok, M., D. Menemenlis, E. Rignot, and M. Studinger (2012), Sensitivity of the ice-shelf/ocean system to the sub-ice-shelf cavity shape measured by NASA IceBridge in Pine Island Glacier, West Antarctica, *Ann. Glaciol.*, *53*, 156–162.
- Schoof, C. (2007), Ice sheet grounding line dynamics: Steady states, stability and hysteresis, *J. Geophys. Res.*, *112*, F03S28, doi:10.1029/2006JF000664.
- Stanton, T. P., W. J. Shaw, M. Truffer, H. F. J. Corr, L. E. Peters, K. L. Riverman, R. Bindschadler, D. M. Holland, and S. Anandkrishnan (2013), Channelized ice melting in the ocean boundary layer beneath Pine Island Glacier, Antarctica, *Science*, *341*, 1236–1239.
- Thurnherr, A. M. (2010), A practical assessment of uncertainties in full-depth velocity profiles obtained with Teledyne/RDI Workhorse Acoustic Doppler Current Profilers, *J. Atmos. Oceanic Technol.*, *27*, 1215–1227.
- Thurnherr, A. M. (2011), Vertical velocity from LADCP data, *Current, Waves and Turbulence Measurements (CWTM), 2011 IEEE/OES 10th*, doi: 10.1109/CWTM.2011.5759552.
- Tortell, P. D., M. C. Long, C. D. Payne, A.-C. Alderkamp, P. Dutrieux, and K. R. Arrigo (2012), Spatial distribution of pCO<sub>2</sub>, DeltaO<sub>2</sub>/Ar and dimethylsulfide (DMS) in polynya waters and the sea ice zone of the Amundsen Sea, Antarctica, *Deep Sea Res., Part II*, *71–76*, 77–93.
- Visbeck, M. (2002), Deep velocity profiling using lowered acoustic Doppler current profilers: Bottom track and inverse solutions, *J. Atmos. Oceanic Technol.*, *19*, 794–807.